

Beyond the Local Volume: Surface Densities of Ultracool Dwarfs in Deep HST/WFC3 Parallel Fields

CHRISTIAN AGANZE,¹ ADAM J. BURGASSER,¹ MATHEW MALKAN,² CHIH-CHUN HSU,¹
CHRISTOPHER A. THEISSEN,¹ DANIELLA C. BARDALEZ GAGLIUFFI,³ RUSSEL RYAN,⁴ AND
BENNE HOLWERDA⁵

¹*Department of Physics, University of California, San Diego, CA 92093, USA*

²*Department of Physics & Astronomy, University of California, Los Angeles, CA 90095, USA*

³*Department of Astrophysics, American Museum of Natural History, Central Park West at 79th Street, NY 10024, USA*

⁴*Space Telescope Science Institute, 3700 San Martin Dr., Baltimore, MD 21218*

⁵*Department of Physics and Astronomy, 102 Natural Science Building, University of Louisville, Louisville KY 40292, USA*

ABSTRACT

[will fill in this after all edits]

1. INTRODUCTION

The structure and evolution of the Milky Way is probed by specific and homogeneous populations of stars. The Milky Way stellar density profile is smooth, fit to an exponential disk component and a power-law or flat spheroid for halo component (Jurić et al. 2008). Ultracool dwarfs (UCDs; $M \lesssim 0.1 M_{\odot}$, $T_{\text{eff}} \lesssim 3000\text{K}$; Kirkpatrick 2005) provide a new approach for studying the Galaxy as they are abundant in every environment throughout the Galaxy. UCDs are members of the late-M, L, T and Y spectral classes, and constitute $\sim 50\%$ of the total number of stars in the galaxy (Cruz et al. 2007, Chabrier & Baraffe 2000, Burrows et al. 2001, Bochanski et al. 2010). They have distinct spectra shaped by strong molecular absorption that are highly sensitive to their temperature, surface gravity and metallicity. In addition, these objects do not fuse hydrogen, hence, they cool down with time. This evolution of UCDs provides potential age diagnostics that have been exploited in stellar

cluster studies (Basri 1998; Luhman & Mamajek 2012; Martin et al. 2017) and searches of young moving groups near the Sun (Lopez-Santiago et al. 2006, Gagné et al. 2015, Mamajek 2015, Faherty et al. 2018).

UCDs are usually discovered in red optical and infrared sky surveys (DENIS: Delfosse, X. et al. 1999, 2MASS: Cruz et al. 2007; Kirkpatrick et al. 2010, WISE: Kirkpatrick et al. 2011; Cushing et al. 2011, UKIDSS: Marocco et al. 2015; Day-Jones et al. 2013; Burningham et al. 2013, CFBDS: Reyle et al. 2010, Gaia: Reylé 2018) but due to their intrinsic faintness, these samples are distance limited (≤ 100 pc). Hence, efforts to constrain the luminosity function have focussed on compiling volume-limited samples of UCDs within 20–25 pc of the sun (Cruz et al. 2007; Metchev et al. 2008; Reyle et al. 2010; Kirkpatrick et al. 2019; Bardalez Gagliuffi et al. 2019). However, UCDs cool with age; and older, metal-poor T-dwarfs populations are more dispersed into the galactic thick disk and halo (Burgasser et al. 2009; Zhang et al. 2019) hinting to a possible different formation mechanism, possible initial-mass function (IMF) variations (Bastian et al. 2010) or an interesting star-formation history (SFH). To further investigate these scenarios, it is useful to conduct searches of UCDs populations beyond the local volume and further into the thick disk and halo of the Milky Way.

Deep pencil-beam imaging and spectroscopic surveys provide star-count data used to characterize stellar and UCD populations beyond the local volume. A common approach of selecting populations of UCDs, in the context of compiling a homogeneous sample of UCDs for follow-up studies in deep surveys, uses photometric selections anchored on a known sample of UCDs. Early work by Gould et al. (1997) sought to infer the dark matter content of the halo by measuring the halo luminosity function of the Hubble Space Telescope’s Wide Field Camera 2 (HST-WFC2) and Planetary Camera (PC1) deep fields. They found 47 M dwarfs with $M_V > 13.5$ consistent with a turning point in power law the mass function at $M \sim 0.6 M_\odot$ from $\alpha = -1$ to $\alpha = 0.44$. Subsequent studies by Kerins (1997); Chabrier & Mera (1997) concluded that the contribution of low-mass stars ($M \sim 0.3 M_\odot$) to the halo luminosity function is less than 1%. Later work by Reylé & Robin (2001) compiled star-count data from different shallow and deep fields surveys and derived a scale height of 800 pc and a scale length

of 2500 pc, and a local density of 10^{-3} pc^{-3} for stellar masses of $0.2\text{--}0.8 M_{\odot}$ consistent with a mass function $\frac{dN}{dM} = M^{-0.5}$.

In the context of using a sample of distant UCDs to probe galactic structure, [Ryan Jr. et al. \(2005\)](#) searched 15 deep parallel fields from the Hubble Space Telescope star-count data and estimated a scale of ~ 350 pc for L & T dwarfs. Later work by [Ryan et al. \(2011\)](#) found 17 late M, L and T dwarfs in 231.90 arcmin^2 of WFC3 imaging of the GOODS fields using a combination of wide and narrow-band filter colors. They estimated a disk scale height of $290 \pm 39 \text{ pc}$ consistent with work by [Pirzkal et al. \(2005\)](#). In addition to poor estimate of spectral types, these samples were contaminated with various non-stellar sources that could not be identified in the absence of spectral information. To push towards a larger and pure sample, [Holwerda et al. \(2014\)](#) identified 274 in 227 arcmin^2 M-dwarfs (to a limiting magnitude $F125W=25$) from the HST-WFC3 Brightest of Re-ionizing Galaxies (BoRG, [Pirzkal et al. 2009](#)) survey, using an optical and near-infrared colors and determined their spectral types using V-J color-M-dwarf subtype relation ([Pirzkal et al. 2009](#)). They found a slightly higher density of M-dwarfs identified in the Northern fields compared to the Southern Fields, and a disk scale-height of $0.3\text{--}4 \text{ kpc}$ with a dependence on subtype. The overall M-dwarf scale height was ~ 600 pc, a number that is much larger than previous estimates mostly due to large uncertainties in the fit. [Van Vledder et al. \(2016\)](#) reanalyzed these data using a Markov Chain Monte Carlo method to fit the statistic to a galactic model including a thin disk, thick disk, and halo component. They derived a scale height of $290^{+20}_{-19} \text{ pc}$ and a central number density of $0.29^{+0.20}_{-0.13} \text{ pc}^{-3}$, with no correlation of model parameters with M-dwarf subtype, and consistent with previous studies. However, these studies do not probe statistics for later types. Recent work by [Sorahana et al. \(2018\)](#) found 3665 L dwarfs brighter than $z=24$ by searching 130 square degrees of the Hyper Suprime-Cam Subaru Strategic Program data and found an average L-dwarf scale height of $340\text{--}420$ pc. [Carnero Rosell et al. \(2019\)](#) compiled a list of 11,745 photometrically classified L0-T9 dwarfs distances up to ~ 400 pc by searching $\sim 2,400 \text{ deg}^2$ of the Dark Energy Survey (DES) data at a limiting magnitude of $z=22$. They estimated a large scale height of ~ 450 pc. These last two studies provide another constraint on the number density of L dwarfs in the Galaxy using large samples ($N > 10^3$); however, as

in many imaging surveys, poor accuracy in spectral types significantly affects the derived parameters. Ultimately, the large uncertainties on spectral types of UCDs in imaging surveys poorly constrain their distances, and deep spectroscopic follow-up of these sources is not a priority for precious HST time.

A parallel approach is to use pencil beam sample of spectra in red optical and near infrared (NIR) with no prior selection of source type. NIR spectroscopy, in particular, samples the peak of UCD spectral energy distribution and broad molecular features that guide UCD classification schemes (Kirkpatrick 2005, Burgasser et al. 2006). Pirzkal et al. (2005) identified 18 M and 2 L dwarfs in the Hubble Ultra Deep Field (HUDF) and estimated their spectral types by fitting templates from Kirkpatrick et al. (2000) to their Gradient-Assisted Photon Echo Spectroscopy (GRAPES) spectra in the optical wavelength regime. This study estimated a disk scale height of 400 ± 100 pc for M and L dwarfs. Another study by Pirzkal et al. (2009) used deep Advanced Camera for Surveys (ACS) slitless grism observations of the Probing Evolution And Reionization Spectroscopically (PEARS) fields (as part the Great Observatories Origins Deep Survey (GOODS) fields, Giavalisco et al. 2004) down to a $z=25$ and spectroscopically identified 43 M4-M9 dwarfs. Using a thick and thin disk model, the study estimated a scale height for the thin disk of ~ 370 pc, and ~ 100 pc for the thick disk, a halo fraction between 0.00025–0.0005 consistent with previous estimates.

Masters et al. 2012 discovered 3 late T dwarfs the WFC3 infrared Spectroscopic Survey (WISPS) fields (Atek et al. 2010) identified by their strong CH_4 and H_2O absorption features. The sample size was not large enough to put meaningful constraints on the scale height or the luminosity function L and T dwarfs beyond the local volume. In this paper, we expand upon this study by developing an effective method to select UCDs in similar surveys.

Section 2 describes the data, section 4 describes the selection process, section 5 discusses the result compared to a Monte-Carlo simulation

2. DATA

2.1. Survey Data

We obtained data from two pure-parallel surveys: the WFC3 Infrared Spectroscopic Parallel Survey (WISPS, [Atek et al. 2010](#)) and 3D-HST ([Momcheva et al. 2016](#), [Brammer et al. 2012](#), [Skelton et al. 2014](#)). These two surveys used the IR channel of the WFC3 camera ([Kimble et al. 2008](#)) providing low-resolution G102 ($\lambda = 0.8\text{--}1.17\ \mu\text{m}$, $R\sim 210$) and G141 ($\lambda = 1.11\text{--}1.67\ \mu\text{m}$, $R \sim 130$) grism spectra. Removal of the slit mask allows for the overlapping spectra of the 136×123 arcsec inner FOV of the WFC3 camera. The WISP survey is a 1000-orbit HST parallel survey covering 390 fields ($\sim 1500\ \text{arcmin}^2$) that follows observing programs accepted on the Cosmic Origins Spectrograph (COS) and Space Telescope Imaging Spectrograph (STIS). 3D-HST is also a parallel survey of 248-orbits spanning $\sim 600\ \text{arcmin}^2$ as part of Hubble Cycles 18 & 19. This survey targets four extragalactic fields: The All-wavelength Extended Groth Strip International Survey (AEGIS, [Davis et al. 2007](#)), Cosmic Evolution Survey (COSMOS, [Scoville et al. 2007](#)), Ultra-Deep Survey (UKIDSS-UDS, [Lawrence & Others 2007](#)), the Great Observatories Origins Deep Survey (GOODS-South and GOODS-North, [Giavalisco et al. 2004](#)), using the ACS/G800L and WFC3/G141 grisms in parallel. Figure ?? shows an WCF3 exposure of one of fields in WISP.

Both surveys provide photometry information from various surveys and instruments in narrow-band and broad-band filters; we used photometric data acquired using F110W, F140W, F160W filters. Figure 7 displays these filter profiles to other standard filters. We report a detailed list observations for all the fields in Table ?? as well as a sky map of all the pointings.

2.2. Data Reduction

Data reduction for the WISP survey is performed using the AXe software Cookbook ([Kuntschner et al. 2013](#); [Kümmel et al. 2009](#)) and a custom pipeline described by [Atek et al. \(2010\)](#); we did not perform any further reduction the both the spectroscopic data or the images provided by the survey. The data 3D-HST Survey deviates from the pipeline AXe pipeline and implements a full custom reduction pipeline. We used data products described by [Momcheva et al. \(2016\)](#) and the photometric catalog of sources in [Skelton et al. \(2014\)](#) retrieved from <https://3dhst.research.yale.edu/Home.html>

3. CALIBRATION SAMPLES

SpeX—We curated a sample of well-known UCD spectra with similar resolution and wavelength region to create our selection methods and quantify their efficiencies and biases. The SpeX dataset is a sample of 2698 M0-T9 low-resolution ($\sim 75\text{--}120$), NIR ($0.9\text{--}2.5\ \mu\text{m}$) spectra of nearby brown dwarfs. We refer to this sample as templates/SpeX sample. These data are stored in the SpeX Prism Library (SPL, Burgasser 2014a, <https://cass.ucsd.edu/~ajb/browndwarfs/spexprism/library.html>) and with SNR >60 . The data were acquired over the last ~ 10 years.

Augmented SpeX dataset—We augmented the SpeX dataset, for machine-learning classification and selection function estimation purposes, to obtain an even larger dataset over 3 orders of magnitude in SNR. We chose at most 10 spectra per spectral type, and added Gaussian noise each spectrum for an iteration of 10^3 steps, yielding 59030 spectra with SNR-J of $10^{-1}\text{--}10^3$.

Manjavacas & Schneider sets—In addition, we compiled a list of UCDs spectra taken with the same instrument. We used the 77 with spectral types $\geq \text{M0}$ objects including UCDs from Manjavacas et al. (2018) observed with WFC-3 as part of a program to study cloud properties of hot jupiters and brown dwarf atmospheres. These data were taken by the G141 grism $1.10\text{--}1.69\ \mu\text{m}$ and have a resolution of $R=\lambda/d\lambda$ 130. The Schneider dataset is a list of 22 Y dwarfs obtained by Schneider et al. (2015) using the WFC3 camera with the same resolution and wavelength coverage. These objects were targeted as a part of a program to determine spectroscopic markers of the T/Y dwarf transition.

4. SELECTION OF UCDS

4.1. *F-test and SNR cuts*

The 3D-HST survey is designed to measure accurate redshifts from emission lines, hence the spectra obtained from the data not continuum-corrected as shown in Figure 7. We obtained a correct continuum of each 3D-HST spectrum by dividing the flux of the spectrum and the sensitivity curve of the detector provided in the data. In addition, we fitted each spectrum to UCDs SpeX spectra of spectral standards using χ^2 minimization following the method of Kirkpatrick et al. (2010) to obtain a preliminary spectral type classification all available WISP and 3D-HST spectra. We also compared every spectrum to a straight line in the same wavelength region and measured χ^2 . The χ^2 of a line

(1) or a standard (std) is given by

$$\chi^2(1, \text{std}) = \sum_{\lambda=1.15\mu\text{m}}^{1.65\mu\text{m}} \frac{(R(\lambda) - \text{Sp}(\lambda))^2}{\sigma_{sp}^2} \quad (1)$$

where $R(\lambda)$ is the reference spectrum (spectral standard or line), $\text{Sp}(\lambda)$ is a WISP or 3D-HST spectrum and σ_{sp}^2 is the noise in the WISP or 3D-HST spectrum. We use an F-test as a statistical test to separate noisy/flat spectra from the rest of the sample implemented by `Scipy` Jones et al. 2001– as `scipy.stat.f`. A flat spectrum is defined as having $F(\chi_s^2/\chi_l^2) > 0.5$. An illustration of various types of spectra and their statistics is provided in figure x. We also defined a signal-to-noise ratio in the J-band continuum (SNR-J) in the wavelength region of $1.2 \mu\text{m} \leq \lambda \leq 1.3 \mu\text{m}$ for all the spectra in both surveys. Point sources are identified both catalogs using `Source Extractor`’s stellarity index `CLASS_STAR` $\neq 0$. In summary, we obtained 270436 grism spectra in both surveys that have corresponding photometry in any of the three bands (F110W, F140W, F160W), among these, 194437 spectra are from WISP and 75999 are from 3D-HST and 110506 objects are flagged as point sources, and 46370 point-source objects have a SNR-J > 3 . Finally, only 637 point sources with SNR-J > 3 satisfy and F-test criterion > 0.5

4.2. Spectral Indices

UCDs display strong CH_4 and H_2O molecular features in $1.1 \mu\text{m} < \lambda < 1.7 \mu\text{m}$ region (Burgasser 2001), they can be separated from other stellar/galaxy populations using these features. Spectral Indices have traditionally been used to determine spectral types (Tokunaga & Kobayashi 1999, Cushing et al. 2000, Allers et al. 2007, Burgasser et al. 2007). Thus, we defined spectral indices in five wavelength bands: $1.15\text{--}1.20 \mu\text{m}$, $1.246\text{--}1.295 \mu\text{m}$, $1.38\text{--}1.43 \mu\text{m}$, $1.56\text{--}1.61 \mu\text{m}$, or $1.62\text{--}1.67 \mu\text{m}$; denoted by $\text{H}_2\text{O-1}$, J-Cont, $\text{H}_2\text{O-1}$, H-Cont, and CH_4 respectively. Each index is the ratio of the median flux in these bands given by

$$Index = \frac{\langle F(\lambda_1 < \lambda < \lambda_2) \rangle}{\langle F(\lambda_1 < \lambda < \lambda_2) \rangle} \quad (2)$$

tracing the H_2O and CH_4 features as well as the J and H band continuum. We measured uncertainties in each index by random sampling, assuming these uncertainties are Gaussian-distributed.

4.3. Box Selection Criteria

We defined selection criteria using boxes/parallelograms in each of 45 independent, 2D spectral index-spectral index spaces. Ideally, UCDs with similar spectral types will cluster within the same region in these spaces, away from the contaminants while the evolution of H₂O and CH₄ bands with subtype should distinguish classes. We created boxes for each index-index pair subtypes using the SpeX, Manjavacas and Schneider datasets.

We fitted a line to each index-index pair within a subtype, defining the slope/direction of the box: $y=mx+b$. Vertices are defined by pairing of x_0, x_1, y_0 and y_1 computed as

$$(x_{\max}, x_{\min}) = \text{median}(x) \pm 3 \times \text{std}(x) \quad (3)$$

;

$$(y_{\max}, y_{\min}) = m(x_{\max}, x_{\min}) + b \quad (4)$$

;

$$(x_0, x_1) = (x_{\max}, x_{\min}) \pm 0.02 \times (x_{\max} - x_{\min}) \quad (5)$$

$$(y_0, y_1) = (y_{\max}, y_{\min}) \pm 1. \times (y_{\max} - y_{\min}) \quad (6)$$

. These boxes are designed to enclose most of the objects in the subtype and avoid outliers. We used rectangular boxes, for their simplicity, and low-contaminations for subtypes M7–L0, L0–L5, L5–T0, and Y dwarfs where the vertices are determined in the same manner as parallelograms, but instead of fitting a line to the objects, we used a horizontal line. This method provides a simple and automatic prescription for selecting objects in an index-index space.

we assess the effectiveness of this method by defining a completeness and a contamination statistic for each of the subtype group as follows:

$$CP = \frac{TEMP_s}{TEMP_{tot}} \quad (7)$$

$$CT = \frac{WFC3_s}{WFC3_{true}} - 1 \quad (8)$$

where $TEMP_s$ is the number of templates selected by the box, $TEMP_{tot}$ is the total number of SpeX templates, $WFC3_s$ is the number of WISPS and/or 3D-HST spectra selected by the box, $WFC3_{true}$ is the number of previously known UCDs in WISPS and /or 3D-HST after visual confirmation. We only employed criteria with the lowest contamination and highest completeness to select UCDs.

We used this selection process iteratively i.e., we first applied the best box for each subtype, that is the box with lowest contamination and highest completeness, we visually inspected the selected spectra, updating $WFC3_{true}$ through this step. We then recomputed CT and CP for all the boxes and repeat this process until there were no new candidates. As a final step, after all selection has been applied, we visually inspected at all the x candidates to find any objects missed by spectral indices, we further discuss the effects of our selection process in section ???. The best criteria for each of the subtype groupings are summarized in table x. We selected 595 objects in total, 89 with spectral types \geq L0 and 19 confirmed via visual inspection 4.5.

4.4. *Random Forest Classifier*

As an alternative to using rigid boxes, we trained a random forest classifier by deploying `RandomForestClassifier` implementation by `scikit-learn` (Pedregosa et al. 2012) to classify potential UCDs in both surveys. Random forests have been shown to reliably predict M-dwarf subtypes based on colors (Hardegree-Ullman et al. 2019) analogous to spectral indices. In addition, random forests have been proven to perform star-galaxy classification in transient surveys, using photometry alone (Miller et al. 2017). Random forest algorithms use a set of independent decision trees constructed based on a random set of features, they assign a final label by averaging the classifications obtained by each decision tree. Furthermore, random forests are a reliable method used to obtain classification for large datasets, given that the algorithm is relatively fast, and not biased by noisy features. This method was also applied iteratively i.e the as we discovered more objects, we added them into the training set and repeated the process until no new candidates were discovered.

The final training set is composed of 1452 visually confirmed non-UCDs from with WISP 3D-HST surveys, 5000 randomly chosen low-SNR WISP 3D-HST objects with both SNR-J and SNR-H <1 , 130 M7-T9 visually inspected candidates from WISP 3D-HST , 2698 M0-T9 objects from the

SpeX set, 77 objects from the Manjavacas set, 22 objects from the Schneider set, and 1000 randomly chosen objects from the Augmented SpeX set. The total number of objects in the training set is 10379. We labeled these sources using two labels: UCDs, which are objects with spectral types \geq L0, and non-UCDs which are objects with spectral types \leq L0 and/or part of the visually confirmed as non-UCDs. This labeling results in 2539 UCDs and 7840 non-UCDs.

Choosing an appropriate set of features is an important part of designing a good machine learning classifier. By intuition, spectral indices, although they are correlated, are a good set of features to use. We added the signal-to-noise ratio in the J-continuum and H-continuum (SNR-J, SNR), the two χ^2 s and their ratio, and the F-test value as additional features. For missing features, we replaced those values with -99999.9 and scaled all features in the range $[0, 1]$ using `MinMaxScaler`. To test the accuracy of our classifier, we use a procedure similar to that of (Miller et al. 2017). We used 2-fold cross validation score and split the training by 50% and 50% partitions. We computed the accuracy by starting with one index as a feature and then adding additional features. We tracked the accuracy of the classification using cross-validation (CV) scores for each additional feature. With only one spectral index, we achieved a classification score of 75.4%, with all additional features we achieved a CV score of 99.4 %, for which spectral indices were responsible for spectral indices alone were responsible for CV score up to 96.5%. We deployed the classifier on 26370 point-source objects in both surveys with SNR-J>3, classifying 129 sources as UCDs with their spectral classification of \geq L0. We then visually inspected these 397 objects and we found 30 real UCDs among them after visual inspection.

In summary, we have presented two methods for selecting UCDs in deep HST surveys potentially applicable future infrared parallel surveys. Both methods rely on spectral indices defined to trace H₂O and CH₄ features prominent in the NIR band of UCDS. The box selection method is efficient (completeness >90%) but with relatively high contamination rates that could be significantly reduced by eliminating the lowest SNR sources. This method is not effective for selecting very low SNR sources due to large scatter in indices and early M-dwarfs as the absorption features in these wavelength ranges are shallow. However, these spectral indices are designed to selected T-dwarfs with high

accuracy (completeness $>90\%$, contamination $<1\%$). The overall contamination rate of this method for spectral types of L0–L5 is $\sim 78\%$. A second method uses a random forest classifier to distinguish UCDs from other extragalactic contaminants or artifacts with an accuracy score of 99.5% in cross-validation. The overall contamination rate of this method for spectral types of L0–L5 is $\sim 92\%$. Both methods rely on a training set of known UCD samples and can be combined and 19 UCDs were found by both the box selection method and the classifier.

4.5. *Spectral Classification and Visual Inspection*

After visual inspection of all the candidates and removal of remaining contaminants, we compiled a sample of UCDs with accurate spectral types. To determine the spectral type classification of each UCD, we compared each of WISP& 3D-HST UCD to SpeX spectral standards using the lowest χ^2 statistic following the procedure of [Kirkpatrick et al. \(2010\)](#).

In addition to spectral types, we computed photometric distances for all the UCDs using absolute 2MASS J and H relations from [Dupuy & Liu \(2012\)](#). Given that these relations are defined for J and H filters, we inferred similar relations for F110W, F140W, F160W filters using the following steps: we first computed an offset between 2MASS J and H magnitudes and AB Hubble magnitudes¹ by convolving the a SpeX standard for that spectral type with the respective filter. This offset in convolutions is then added to the absolute magnitude-spectral type relations in 2MASS J, H filters to obtain the new relation in Hubble filters. We used these relations throughout this study to determine distances given an apparent F110W, F140W or F160W magnitude and a spectral type.

5. RESULTS

5.1. *M, L, T Dwarfs Candidates*

We found 25 L and T dwarfs. We purposely excluded M-dwarfs in the sample given that H_2O and CH_4 features in these regions are weak. We report their distances and photometry in table 2. We found L-dwarfs up to $\sim 1000\text{pc}$, and T-dwarfs up to $\sim 500\text{ pc}$; the distribution of distances for

¹ 3D-HST F140W and F160W magnitudes are computed using reported fluxes in photometric catalogs in [Skelton et al. 2014](#) as $-2.5 \log_{10} F + 25$, while WISPS magnitudes are used as reported

all the UCDs is shown in Figure ?? and we recovered the 3T-dwarfs discovered by [Masters et al. 2012](#). We found 14 L dwarfs in both surveys, 11 T dwarfs in WISP and 3 L dwarfs in HST-3D, all with a $\text{SNR-J} > 4$. The closet L dwarf in the sample is WISP 0927+6027, with spectral type of L0 at $\sim 320 \pm 10$ pc and a SNR-J of ~ 320 , while the farthest L-dwarf is WISP 1154+193 with spectral type of L3 at a distance of $\sim 1800 \pm 650$ pc. We also found 9 T dwarfs, 7 in WISP and 2 in 3D-HST. WISPS T dwarfs include T7 WISP 1232-0033, T9 WISP 1305-2538 and T4 WISP 0307-7243 found by [Masters et al. 2012](#), and are the latest T dwarfs in the sample. The farthest T dwarf in the sample is UDS 0217-0514 at a distance of 2400 ± 360 pc and with a SNR-J of ~ 9 , the closet T dwarf in the sample is WISP 1232-0033 at a distance of 2400 ± 360 pc and with a SNR-J of 9. AEGIS1418+5242 is the second T dwarf in 3D-HST with a spectral type of T4 and at a distance of 540 ± 80 pc at with a SNR-J of 24.

5.2. Comparison to Predictions

5.2.1. Magnitude Completeness

We aim to constrain the number density of UCDs; an accurate estimate of the effective distance/volume of each pointing is crucial. [Momcheva et al. 2016](#) reported the effective depths of all the pointings in 3D-HST, however, given the SNR cut, we expect the a brighter limit than these reported depths. Hence, we adopted the faintness limits of $F110W=22.0$, $F140W=21.5$, $F160W=21.5$ for WISP fields, and $F140W=22.5$, $F160W=22.5$ for 3D-HST fields. For the bright end, we used the bright limits of $F110W=18.0$, $F140W=16.0$, $F160W=16.0$ for WISPS fields and $F140W=16.0$, $F160W=16.0$ for 3D-HST fields following the peak of the distribution of magnitudes (Figure ??) for all the point sources satisfying the SNR cut. These bright limits correspond to limiting distances hence effective volumes for each spectral type, using the absolute magnitude spectral type relation from [Dupuy & Liu 2012](#)

5.2.2. Selection Function

Because we applied several selection criteria to narrow down our sample for visual confirmation, it is possible we may have missed a few UCDs in the WISPS/3D-HST fields; particularly low SNR

or peculiar objects due, in part, to uncertainties in spectral indices. To fully quantify these effects, we generated a distribution of spectra uniformly sampling our SNR distribution across a wide range of SNRs and measured their recovery rate through this selection process. To simulate a sample for spectra with various SNR-Js, we degraded a sample of chosen spectra from the SpeX sample by selecting at least 20 highest SNR objects in the SpeX sample per spectral type, and added Gaussian noise to these spectra until the overall SNR to noise in the spectrum is reduced below 3.0. We computed all relevant statistics for each of these generated spectra, including SNR-J, spectral indices, F-test, and the two χ^2 s. We applied our selection processes to this sample of simulated spectra by measuring spectral indices and applying first f-test criterion where F-test > 0.5, box index-index selection criteria and the random forest classifier. The fraction of spectra selected per spectral type per SNR bin is defined as the probability of selection of an object within Δ SNR-J bin of 2.0. We denote this probability of selection of $\mathcal{S}(\text{SNR-J, SpT})$

$$\mathcal{S}(\text{SNR-J, SpT}) = \frac{N_s}{N_{tot}}$$

where N_s is the number selected spectral type and SNR bin, and N_{tot} is the total number of objects in that bin.

5.2.3. Number Densities, Monte-Carlo Simulation

To compute the expected number of UCDs in each spectral type bin, we simulated a semi-empirical luminosity function, which we multiply by the effective volume of each spectral type corrected by our selection function. We followed these steps:

- We first simulated a sample of 10^5 objects in a power law mass function for a range of masses 0.02 M_\odot and 0.15 M_\odot as

$$\frac{dN}{dM} = \left(\frac{M}{M_\odot} \right)^{-0.6} \quad (9)$$

normalized to 0.0055 pc^{-3} at $M=0.10 M_\odot$ (Reid et al. 1999, Chabrier 2001)

- We assigned each of these UCDs an age drawn from different star-formation histories: a uniform age distribution spanning 100 Myr–10 Gyr, a range of age exponential age distributions ($\beta \in$

[0.1, 10.0]) given by

$$P(t) \sim e^{\beta t} \quad (10)$$

and two predefined distributions from [Aumer & Binney \(2009\)](#) and cosmic age distribution from [Rujopakarn et al. \(2010\)](#)

- We assigned a temperature using UCD evolutionary models from [Baraffe et al. \(2003\)](#) converted to a spectral types using the relation from [Filippazzo et al. \(2015\)](#). We defined $\Phi(\text{SpT})$ as this normalized distribution of spectral types.
- To account for the effects of galactic structure, we computed an effective volume for each spectral type defined following [Burgasser \(2007\)](#) defined as

$$V_{eff}(\text{SpT}) = \frac{1}{3}(d_{max}^3 - d_{min}^3) \times \Delta\Omega \times V_c \quad (11)$$

. Where $\Delta\Omega$ is the solid angle of the pointing and $d_{max,min}$ are the effective maximum or minimum distances given by

$$\log d_{min,max} = \frac{1}{5}(m - M(\text{SpT})) + 1 \quad (12)$$

. V_c is a volume correction term, to account for the galactic structure obtained by integrating the galactic density as

$$V_c(l, b) = \frac{\int_0^{\delta x} \rho(x, l, b) x^2 dx}{\int_0^{\delta x} \rho_0 x^2 dx} \quad (13)$$

where x is the 3D- galacto-centric distance in along the line of sight of the field, and $\rho(x)$ is the galactic density along that line of sight. We set $\delta x = d_{max} - d_{min}$ as the total depth of a given pointing. We assumed a standard galactic structure model similar from [Jurić et al. \(2008\)](#)

- The spatial density of stars in each pointing is given by

$$\rho(R, z) = \rho_{thin} + \rho_{thick} + \rho_{halo} \quad (14)$$

$$\rho_{thin} = \rho_0 \exp\left(-\frac{|z - Z_\odot|}{H_{thin}}\right) \times \exp\left(-\frac{R - R_\odot}{L_{thin}}\right) \quad (15)$$

$$\rho_{thick} = \rho_0 \times f_{thick} \times \exp\left(-\frac{|z - Z_\odot|}{H_{thick}}\right) \times \exp\left(-\frac{R - R_\odot}{L_{thick}}\right) \quad (16)$$

$$\rho_{halo} = \rho_0 \times f_{halo} \left(\frac{R_\odot}{\sqrt{R^2 + (z^2/q^2)}} \right)^{-p} \quad (17)$$

H_{thin}, H_{thick} are the scale height of the thin and thick disk, L_{thin}, L_{thick} are the scale length of the thin/thick disk, q is the axial ratio the halo sphere, p is the flattening parameter and f_{thick}, f_{halo} are the fraction of stars in the thin thick disk and the halo.

- Given that our selection function is a function of both SNR-J and spectral type, we must assign a SNR-J to the distribution of 10,000 simulated objects. We computed a distribution of distances where the probability is given by

$$P(d_{min} < d < 2 \times d_{max}, l, b) \sim d^3 \times V_c(l, b) \quad (18)$$

where l, b are galactic latitude and longitude. After assigning each simulated UCD a distance, we computed an apparent magnitude using a polynomial to fit \log SNR-J to the absolute apparent magnitudes of the WFC3 UCD sample (Figure x).

- We then used our most selective selection function \mathcal{S} to assign a probability of selection/detection to each of the of the simulated objects.
- The expected number of sources per spectral type is given

$$N_{exp}(SpT) = \rho_0 \times V_{eff}(SpT) \times \sum_i \mathcal{S}_i n_i(SpT) \quad (19)$$

. Where n_i is the number of objects in a spectral type bin and \mathcal{S}_i is the probability of selection for each object in that spectral type bin. We compared these numbers to the observed numbers of UCDs for each age distribution in figure 20

6. SUMMARY & DISCUSSION

The measured number of T-dwarfs is consistent with expectations given atmospheric cooling effects (Burgasser 2004) from evolutionary models. As UCDs age, they quickly pile up on at the lower end of the spectral type distribution and cooler temperatures. Ryan et al. (2017) estimated a change in scale height of ($\Delta H \sim 50$ pc) in the mid-L dwarf regime by comparing galactic models for different cooling scenarios; while the scale height in for M-dwarf remains constant independent of subtype. Despite the high accuracy in spectral types for the sample of UCDs presented in this study, the small sample of size of 20 could not accurately constrain the scale height for each spectral type.

Moreover, the L/T transition region is sensitive to unresolved binaries (Bardalez Gagliuffi et al. 2014). Burgasser (2007) shows that given a spectral binary fraction of $\sim 10\%$, the surface densities for volume-limited sample of primaries and combined systems are similar but present a slight bump ($\Delta \Sigma \lesssim 5 \times 10^{-5} \text{ deg}^{-2}$) for early T dwarfs. Given our total search area of $\sim 0.6 \text{ deg}^2$, we do not expect a significant effect of the spectral binary fraction to the reported densities, hence we assumed that none of the UCDs in this study are unresolved binaries in our simulation.

Metallicity effects affect the number of subdwarfs we expected in this sample. UCDs in the thick disk and the halo have similar kinematic ages with stellar populations in these parts of the Galaxy; and UCDs at different metallicities follow different evolutionary tracks. L subdwarfs in the local neighborhood are therefore rare, and this study does not significantly probe large volumes in the thick disk and halo. Lodieu et al. (2017) found $0.04 \times \text{deg}^{-2}$ L subdwarfs in the UKIDSS/SDSS fields; in fact, we expect the number of subdwarfs to be ~ 400 times lower than the expected number of dwarfs in the sample. Although the parallel fields in 3D-HST & WISP are deep, the total search area remains low, hence it is not surprising that we did not find any L subdwarfs in the sample.

Future space missions such as JSWT, Euclid will be contaminated by UCDs. Ryan Jr. & Reid (2016) predicted that the number density of UCDs (M8–T8) in JSWT fields peaks around $J \sim 24$ mag with a total surface density of $\Sigma \sim 0.3 \text{ arcmin}^{-2}$. With the *Large-Scale Synoptic Telescope* (LSST), and the *Wide-Field Infrared Survey Telescope* (WFIRST), we expect an increase in both sample size and spectral type accuracy, expanding the parameter space necessary to put significant constraint on

the star formation history of the Milky Way in general and the mass function of UCDs in particular (LSST Science Collaboration et al. 2009, Spergel et al. 2015).

Acknowledgment for WISPS

This work is based on observations taken by the 3D-HST treasury program (GO 12177 and 12328) with the NASA/ESA HST, which is operated by the Association of universities for Research in Astronomy, Inc. under NASA contract NAS5-26555.

CA thanks the LSSTC Data Science Fellowship Program, which is funded by LSSTC, NSF Cyber-training Grant #1829740, the Brinson Foundation, and the Moore Foundation; his participation in the program has benefited this work.

Software: Astropy (Collaboration et al. 2013), Matplotlib, SPLAT (Burgasser 2014b), Scipy, Pandas, Seaborn

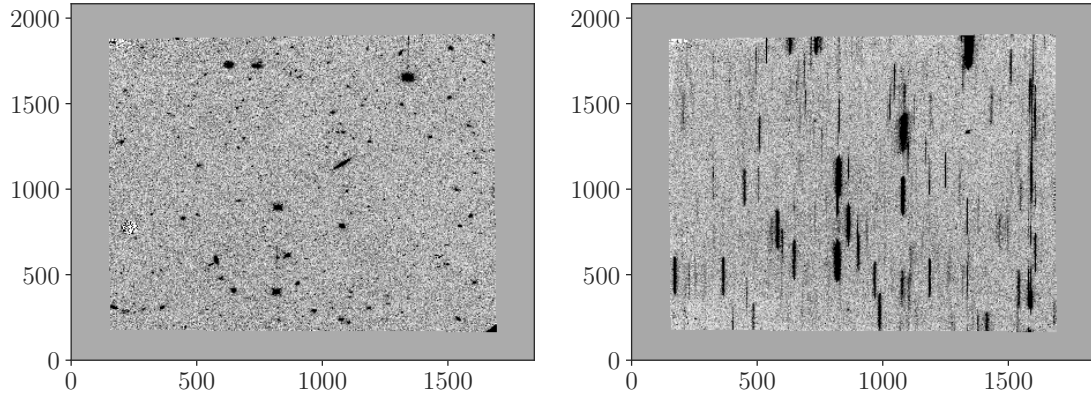


Figure 1. Example of a reduced grism spectrum of WISPS-01

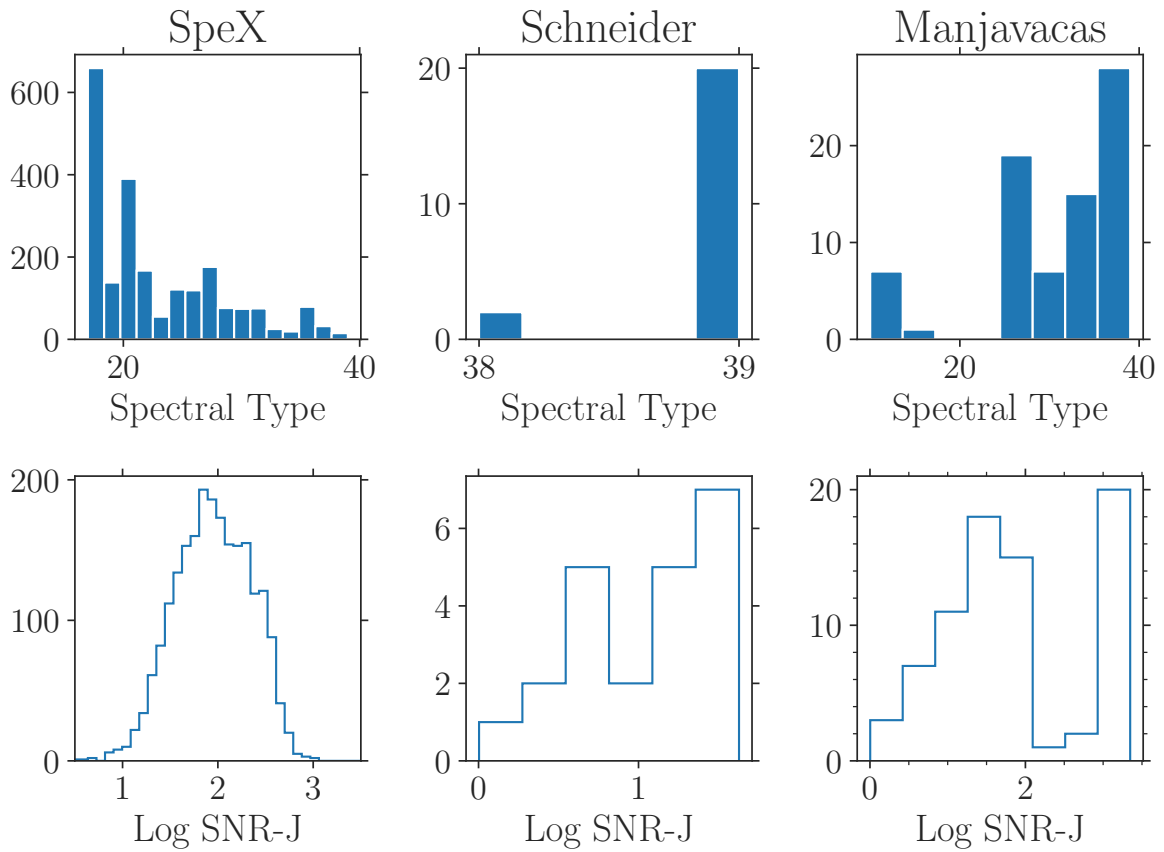


Figure 2. Calibration Samples of UCDs used in this study

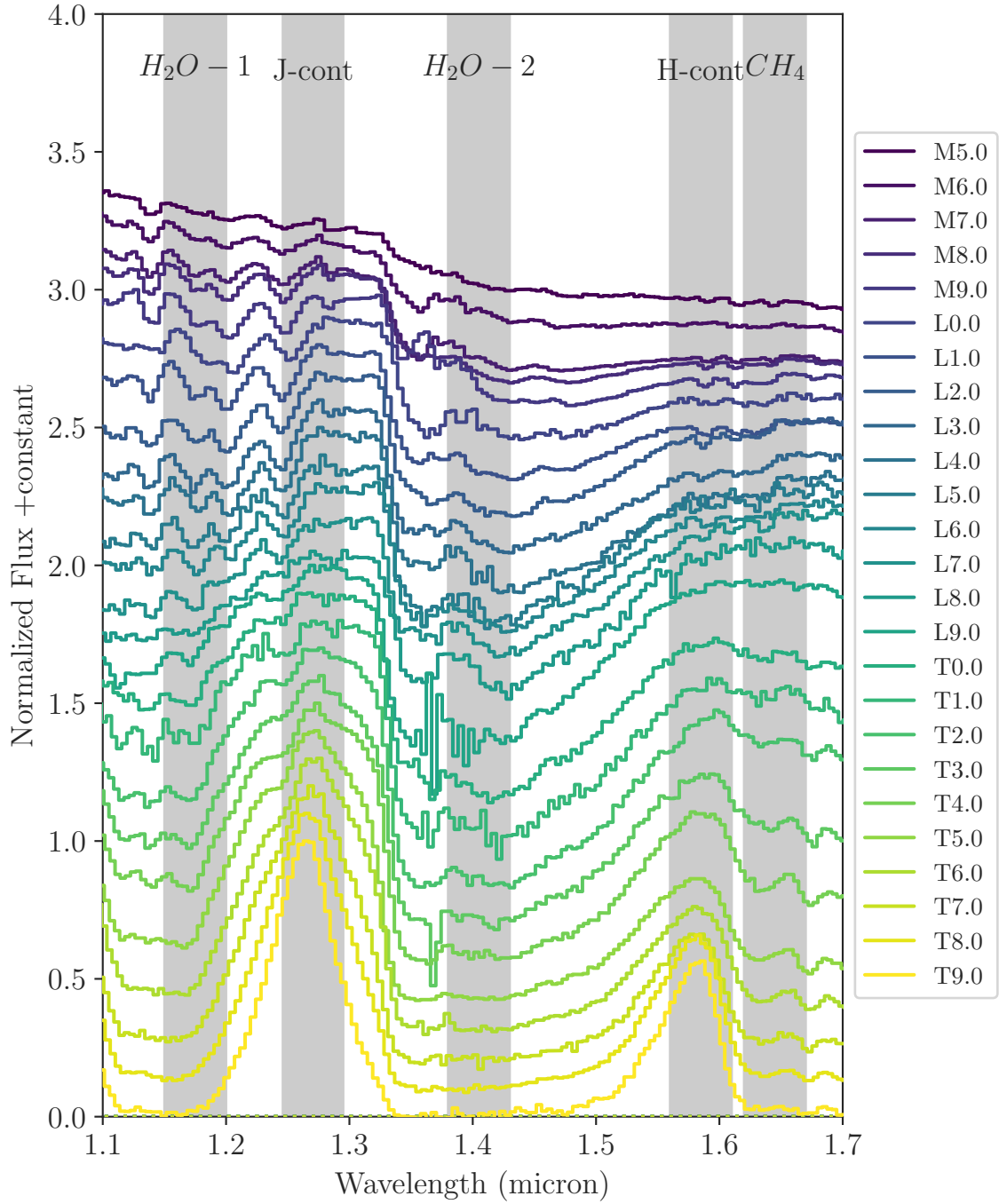


Figure 3. M5-T9 low resolution SpeX spectral standards (Kirkpatrick et al. 2010) with highlighted bands showing the definition of spectral indices used in this study

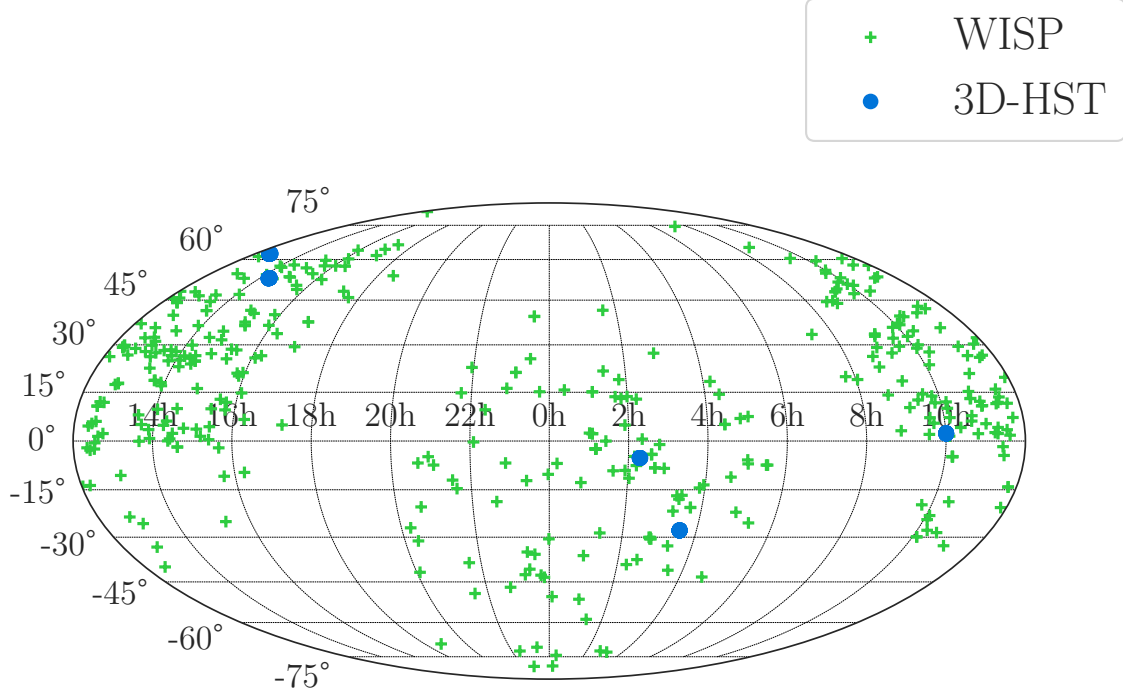


Figure 4. Sky map of all the pointings in WISPS and 3D-HST

Table 1. Best Selection Criteria

SpT Range	X-axis	Y-axis	m	b	s	Completeness	Contamination
L0–L5	H-cont/ H_2O -1	CH_4 $/J - cont$	0.0	1.0	0.6	0.99	0.14
L5–T0	H-cont/ H_2O -1	H_2O -2/ $J - cont$	0.17	0.29	0.39,	0.95	0.165
T0–T5	CH_4 $/H_2O$ -1	H_2O -2/ $J - cont$	-0.1	0.28	0.43	0.93	0.135
Y dwarfs	H_2O -2/ $J - cont$	CH_4 $/H - cont$	1.21	0.09	0.19	0.89	0.003
T5–T9	H_2O -1/ $J - cont$	CH_4 $/H - cont$	1.61	0.03	0.09	0.95	0.003
Subdwarfs	H-cont/ $J - cont$	CH_4 $/J - cont$	1.05	-0.01	0.04	0.9	0.031

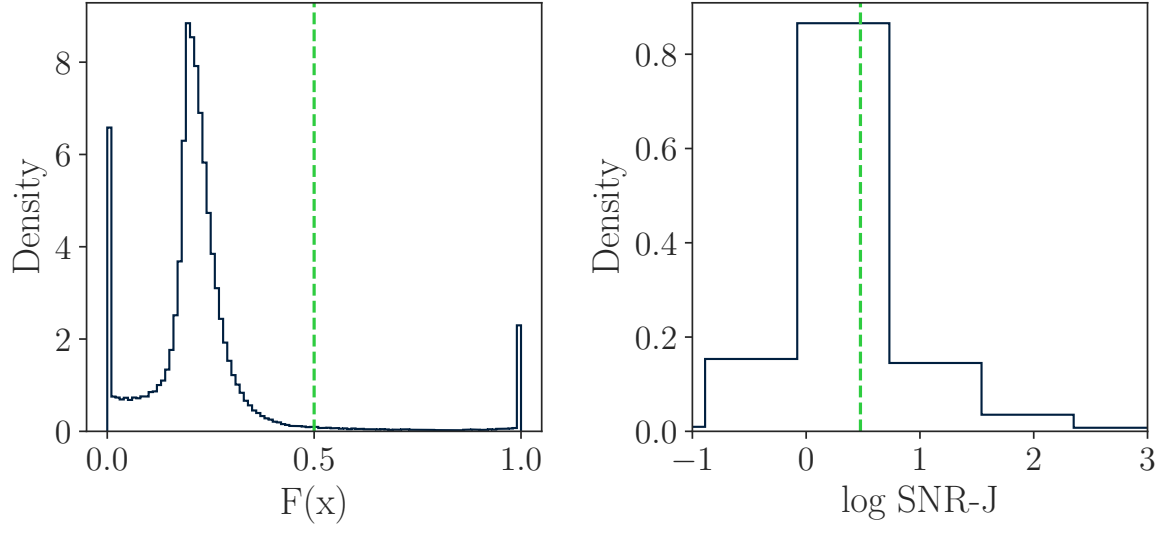


Figure 5. f-test and SNR-J distributions of all Spectra in both surveys

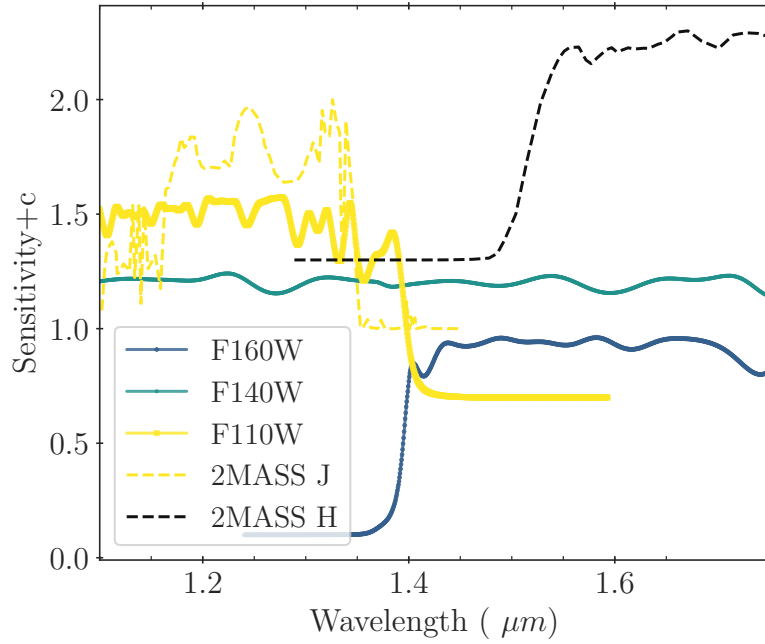


Figure 6. Comparison between different HST and 2MASS filters used in this study

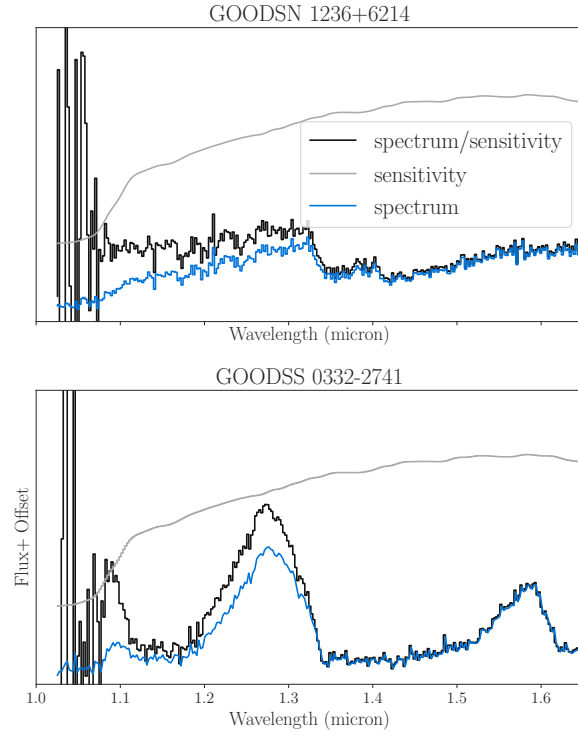


Figure 7. Example of 2 HST-3D spectra before and after continuum correction to obtain the correct slope. The sensitivity curve is plotted in grey.

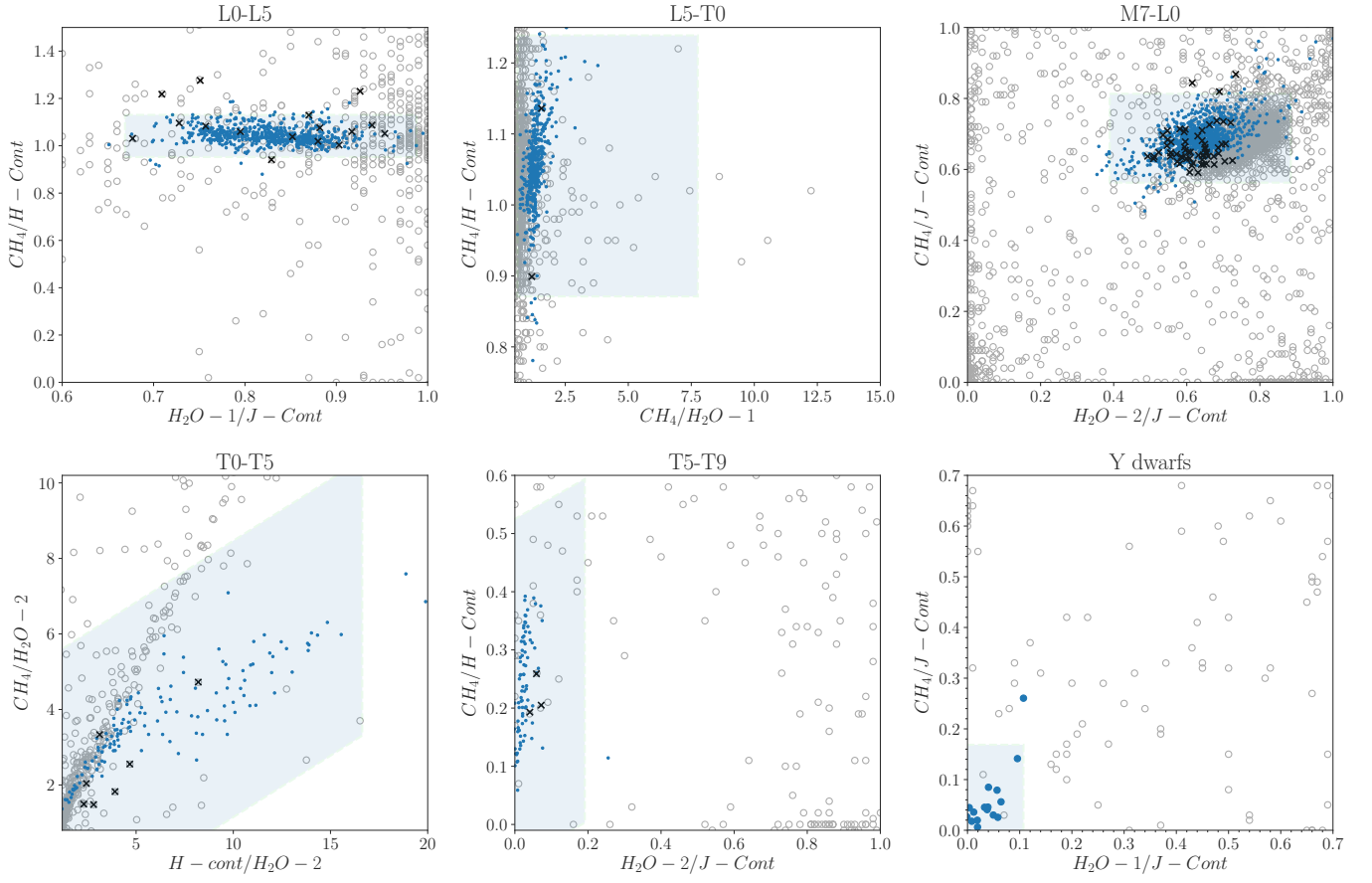


Figure 8. Best selection criteria for different subtype ranges. Both the calibration samples and the contaminants are shown

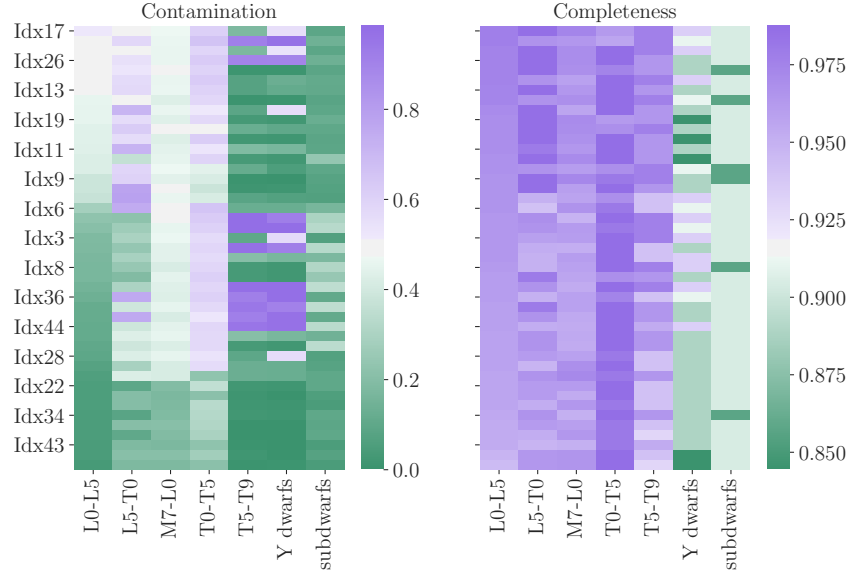
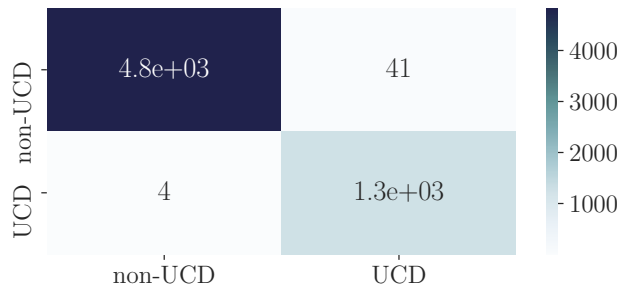
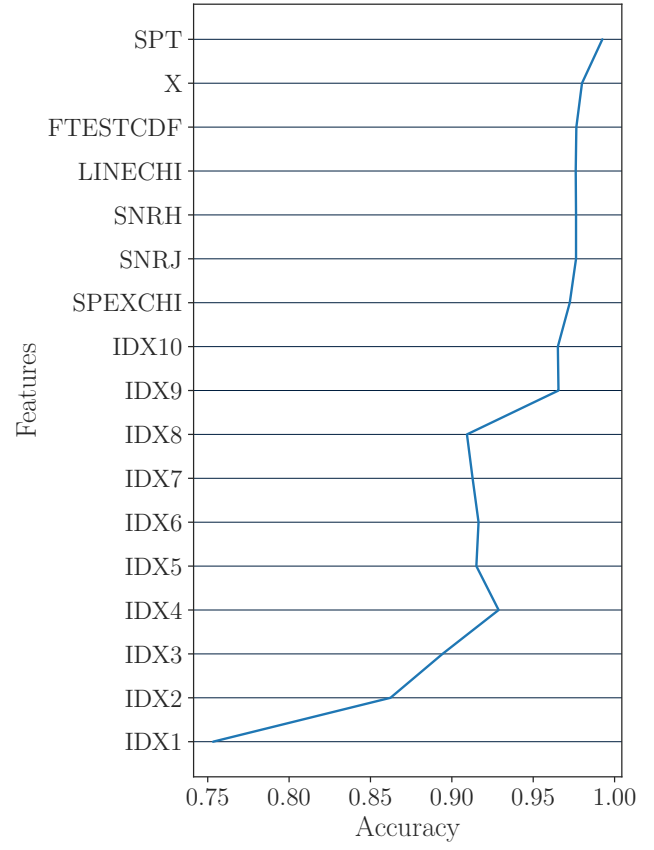


Figure 9. Visual Representation of CPT and COMP statistics for all possible combination of spectral indices for each subtype range. Although the overall completenesses of each box is high ($>80\%$), the contamination may vary. We only use selection criteria with the lowest possible contamination, however, any combination of these indices could be useful for selecting UCDS in other surveys



(a)



(b)

Figure 10. (a) Confusion matrix for the random forest classifier used in this survey (b) CV scores for the number of features used

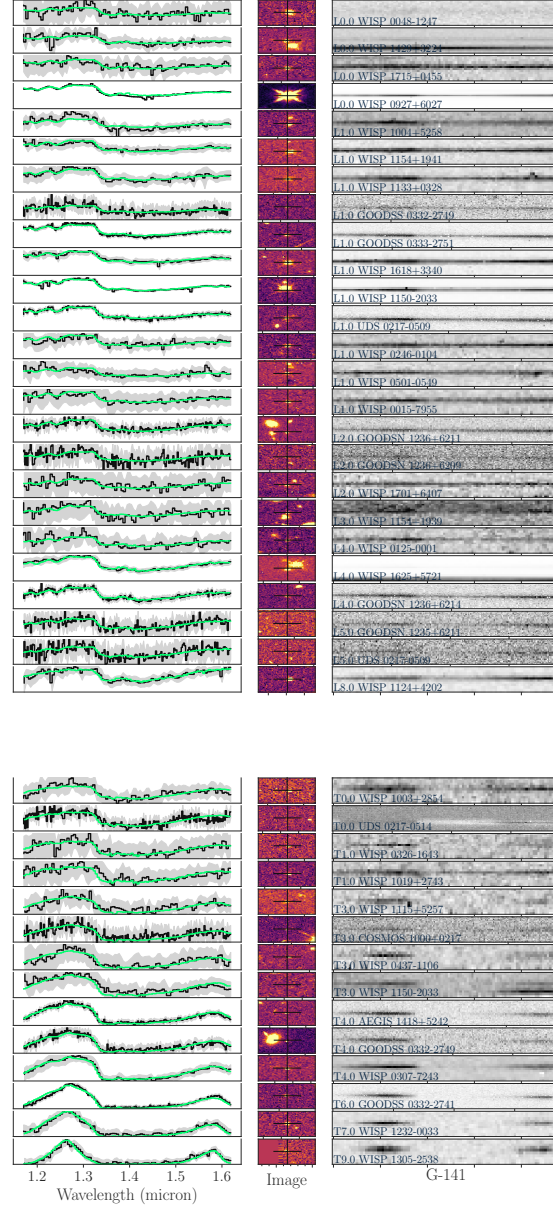


Figure 11. Spectral Sequence of UCDs Discovered in WISPS & 3D-HST. The right plot shows the 1D spectrum where the shaded region is the reported contamination by the survey, the middle plot shows the WFC3 image acquired in either F140W, F160W or F110W filter and the far-left plot shows the cutoff of the G141 spectrum for that extracted object. The derived spectral type of each object is displayed in the left corner of the far-left plot

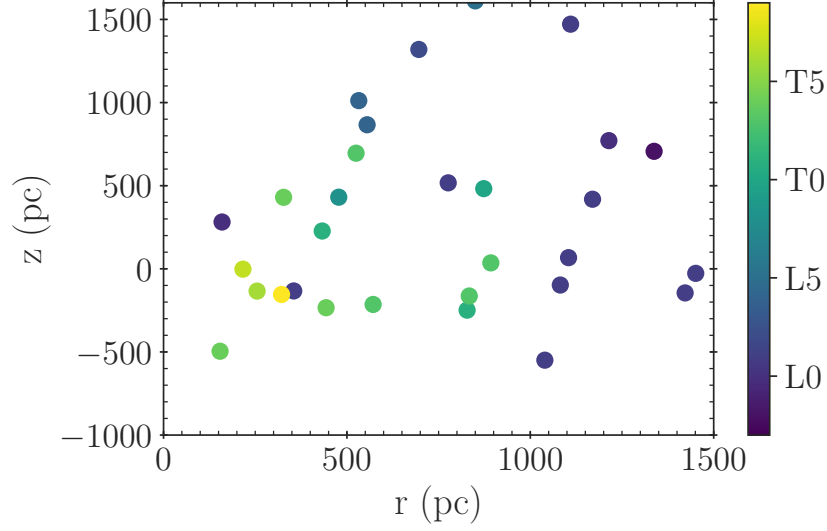


Figure 12. Spatial distribution of the the UCD sample reported in this paper

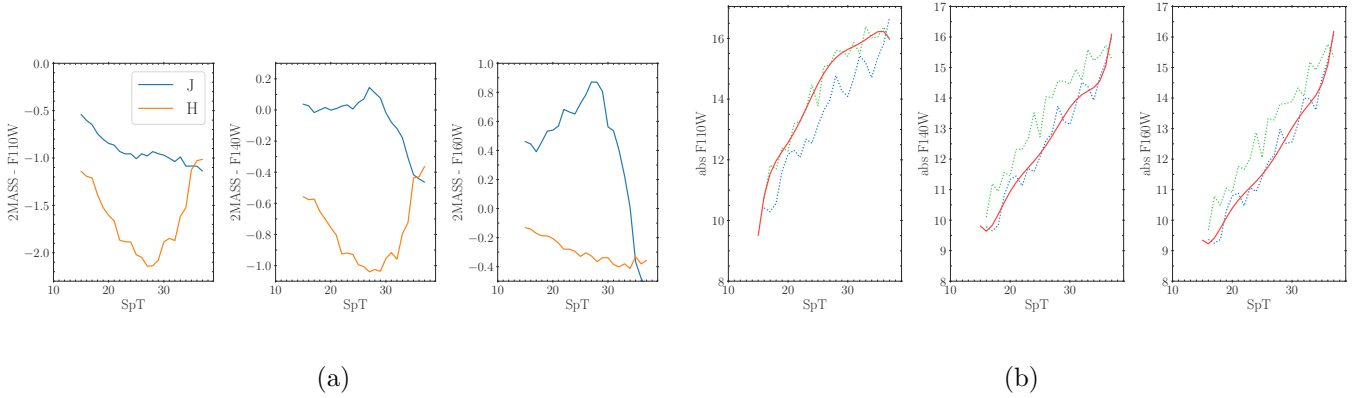


Figure 13. (a) Offsets between 2MASS J, H magnitudes and HST F110W, F140W, F160W magnitudes as a function of spectral type (b) Absolute magnitude-spectral type relations for HST and 2 MASS filters. For HST filters, the dotted green curve shows the derived relation using only the offset between the respective HST filter and 2MASS J filter while the blue curve shows the derived relation using the offset with the 2MASS H filter. The solid line shows a best-fit 6th-order polynomial used, considering the wavelength coverage of the respective filters (figure 6). We report the coefficients of these polynomials in table 3

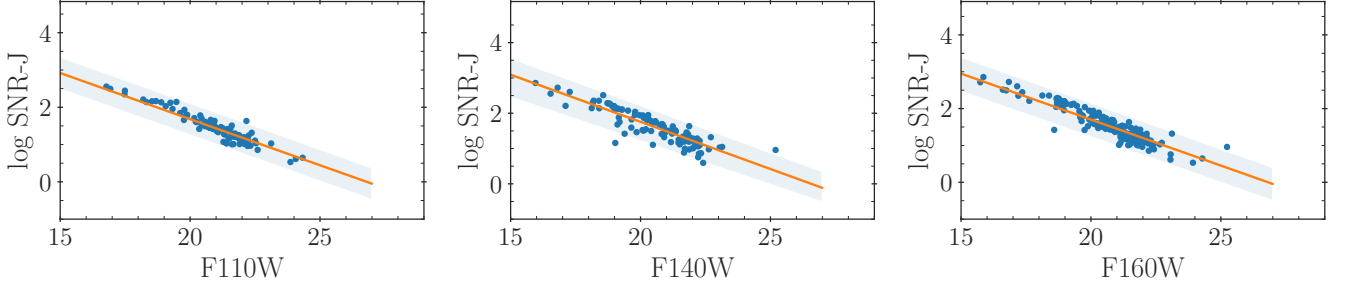


Figure 14. Linear fits between SNR-J and apparent F110W, F140W, F160W magnitudes using the sample of UCDs. These relations are reported in table 3 and used to estimate SNR-J for different apparent magnitudes

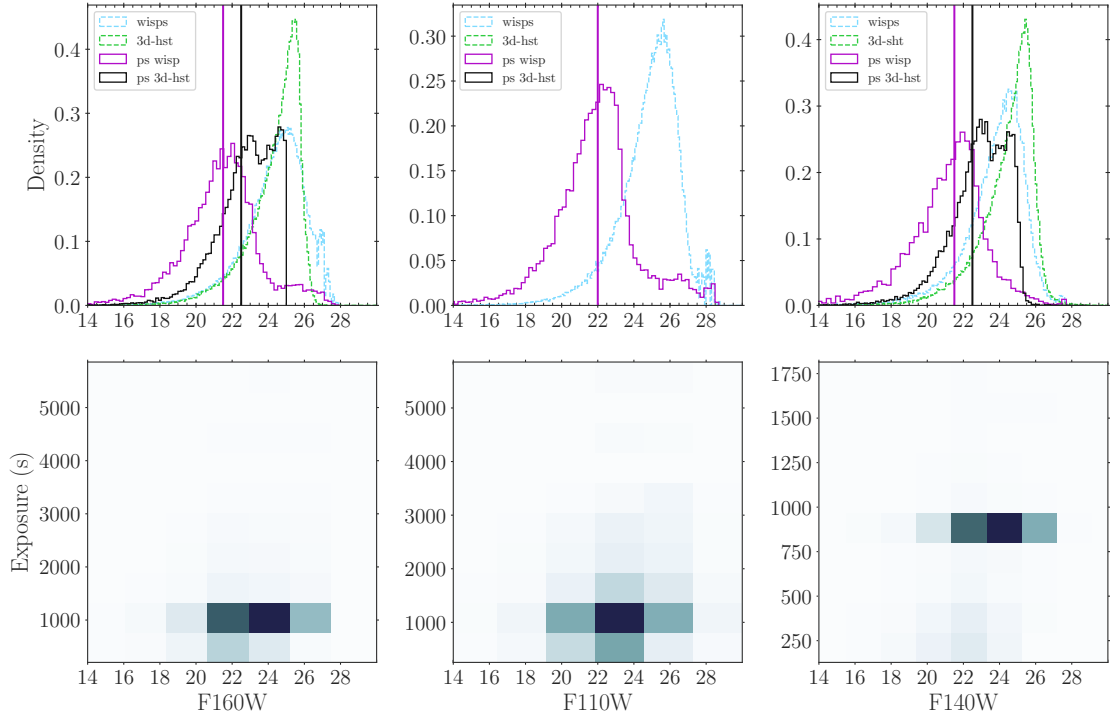


Figure 15. Magnitude distribution of point sources (solid lines) and all the sources (dotted lines) in both WISP & 3D-HST. We estimate the limiting magnitudes based on the distribution of point sources. For wisps the limiting magnitudes are F110W=22.0, F140W= 21.5, and F160W= 21.5. For 3D-HST the limiting magnitudes are F140W=22.5 and F160W. These magnitudes are used to compute the effective volumes for each spectral type

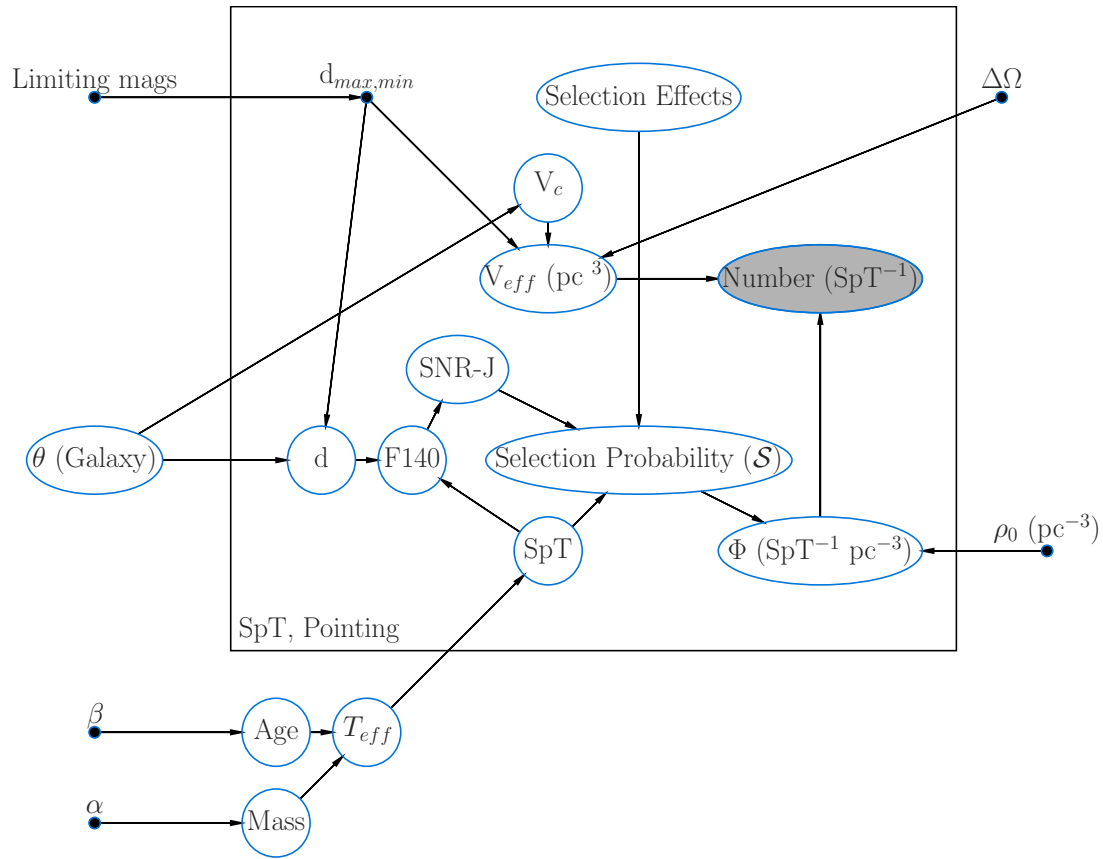


Figure 16. Graphical Model showing the simulation process

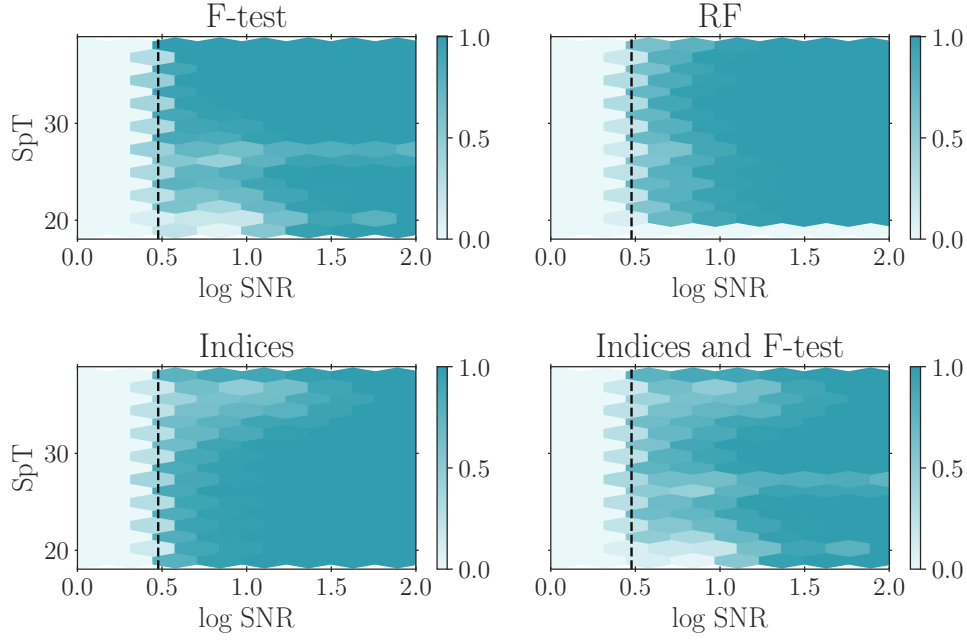


Figure 17. Visualization of our selection function as a function across spectral type and SNR-J. The label "F-test" indicates spectra with F-test > 0.5 , the label "RF" indicates the spectra labelled as UCDs by the random forest classifier, and the label "Indices" indicates the spectra selected by our best selection criteria. The bar indicates the selection probability defined as the number of spectra selected over the total number of spectra in each SNR-J, spectral type bin. In the Monte-Carlo simulation, we use the most-selective selection function.

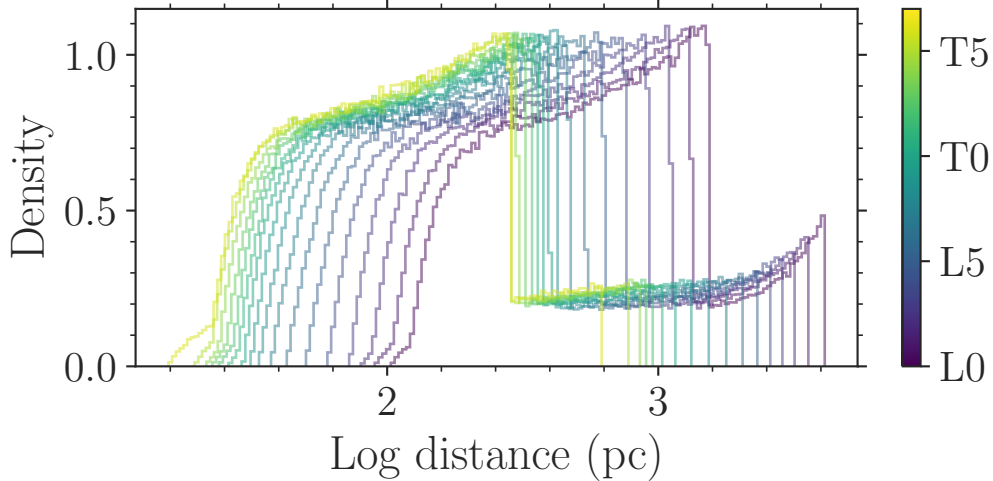


Figure 18. Distribution of randomly drawn distances in all WISPS & 3D-HST pointings [18](#)

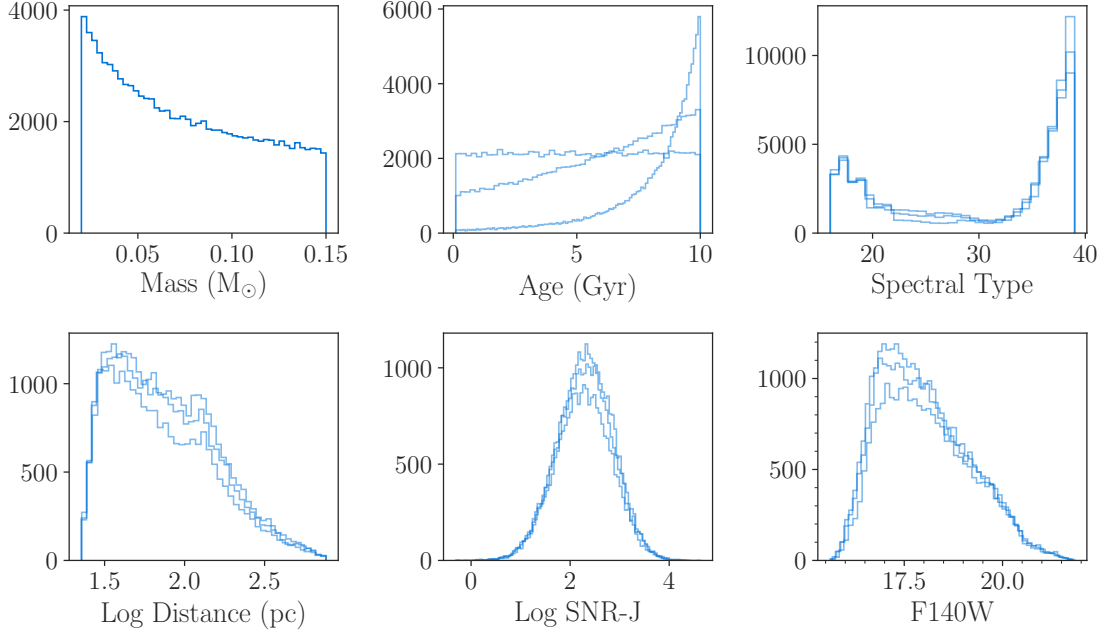


Figure 19. Monte-Carlo simulation: distribution of randomly drawn masses, ages, distances and computed spectral types, SNR-J and apparent F140W following relations defined in this work

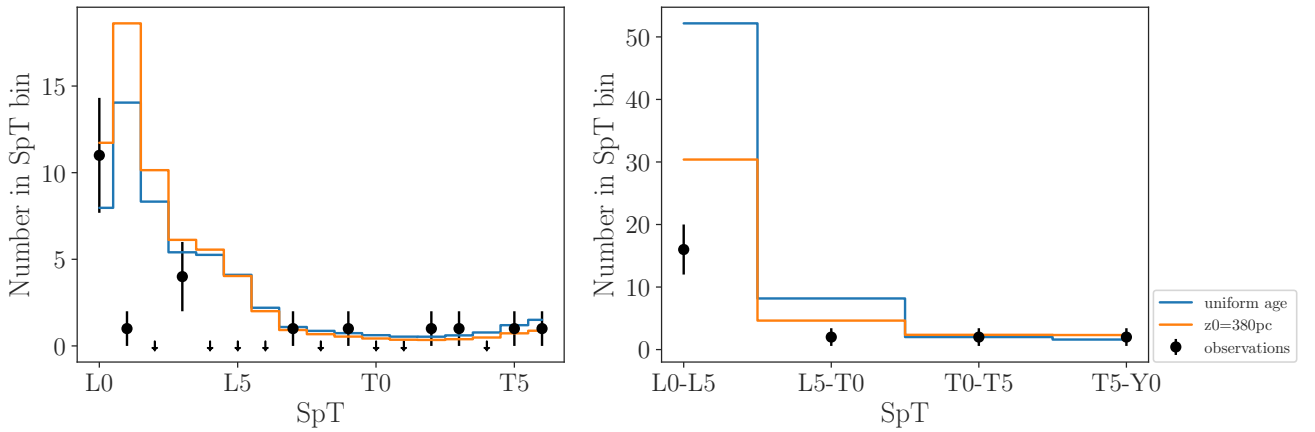


Figure 20. Comparison between the measured number densities and the expected number densities based on the Monte-Carlo simulation based on different age distributions. We observe an under-prediction within Poisson-like errorbars ($\sim \sqrt{N}$) between the predictions and the measurements per subtype but an agreement within subgroupings of 5 subtypes. The total number of predicted UCDs with spectral types \geq L0 is 16.9 while the total number of UCDs within the limiting magnitudes ($F110W > 22.0$ or $F140W > 21.5$) is 16

Table 2. List of L0-T9 UCDs

Short Name	Grism ID	SNR-J	SpT	RA	DEC	F110W	F140W	F160W	Distance (pc)	Distance error
WISP0927+6027	PAR21-00005	324	L0	141.989319	60.462970		18.6		323	7
UDS0217-0509	UDS-25-G141_36758	31	L1	34.318333	-5.153692		21.3	21.0	1086	81
WISP1154+1941	PAR338-00035	13	L1	178.716644	19.684700	22.2		21.9	1242	532
WISP1133+0328	PAR27-00036	10	L1	173.274353	3.477643	21.6	22.0	21.4	1106	407
WISP1618+3340	PAR65-00035	19	L1	244.707458	33.671520	21.7		21.3	933	390
WISP1150-2033	PAR199-00009	57	L1	177.706833	-20.561000		19.2		379	7
WISP1004+5258	PAR438-00051	10	L1	151.204559	52.974800		22.6		1845	32
WISP0015-7955	PAR244-00072	6	L1	3.785810	-79.930220		22.2		1531	27
GOODSS0333-2751	GOODSS-28-G141_10859	34	L1	53.267498	-27.860249		21.4	21.3	1176	154
GOODSN1236+6211	GOODSN-33-G141_09283	12	L2	189.223923	62.188259		22.2	22.0	1491	130
WISP1154+1939	PAR338-00136	4	L3	178.720154	19.660000	24.1		23.1	1809	661
WISP1625+5721	PAR156-00041	19	L4	246.353882	57.357600			21.4	1029	14
GOODSN1236+6214	GOODSN-24-G141_21552	19	L4	189.161880	62.247669		22.0	21.8	1144	125
WISP1124+4202	PAR106-00047	11	L8	171.034760	42.042900			21.5	644	14
WISP1003+2854	PAR191-00077	6	T0	150.918884	28.912800			23.1	996	22
UDS0217-0514	UDS-12-G141_10759	9	T0	34.435657	-5.240000		25.2	25.2	2401	352
WISP0326-1643	PAR467-00135	3	T1	51.511295	-16.722500	23.9		23.9	865	444
WISP1019+2743	PAR201-00044	4	T1	154.888565	27.720400		22.4		489	7
WISP0437-1106	PAR463-00176	4	T3	69.490608	-11.104400	24.3		24.3	850	380
GOODSS0332-2749	GOODSS-04-G141_17402	13	T4	53.161709	-27.831562		22.6	22.9	501	69
WISP0307-7243	PAR130-00092	12	T4	46.921608	-72.732600			22.7	518	11
AEGIS1418+5242	AEGIS-03-G141_17053	21	T4	214.710007	52.716480		22.7	23.1	540	78
GOODSS0332-2741	GOODSS-01-G141_45889	31	T6	53.242542	-27.695446		22.1	22.9	289	52
WISP1232-0033	PAR58-00112	11	T7	188.176712	-0.551850		23.1		218	25
WISP1305-2538	PAR32-00075	11	T9	196.356232	-25.641300	23.1	23.0	22.7	359	495

REFERENCES

- Allers, K., Jaffe, D., Luhman, K., et al. 2007, *\apj*, 657, 511
- Atek, H., Malkan, M., McCarthy, P., et al. 2010, *\apj*, 723, 104
- Aumer, M., & Binney, J. 2009, *\mnras*, 397, 1286
- Baraffe, I., Chabrier, G., Allard, F., & Hauschildt, P. 2003, in IAU Symposium, Vol. 211, Brown Dwarfs, ed. E. Martín, 41–+
- Bardalez Gagliuffi, D., Burgasser, A., Gelino, C., et al. 2014, *\apj*, 794, 143

Table 3. Polynomial relations used in this work where the polynomial is given by $y = \sum_{n=1}^7 c_n x^n$

x	y	Scatter	Coefficients						
			c7	c6	c5	c4	c3	c2	c1
SpT	Abs F110W	0.4	-3.2×10^{-6}	5×10^{-4}	-3.4×10^{-2}	1.15	-2.2×10^1	2.2×10^2	-9×10^2
SpT	Abs F140W	0.4	3.5×10^{-6}	-5.4×10^{-4}	3.4×10^{-2}	-1.1	2×10^1	-2×10^2	7.85×10^2
SpT	Abs F160W	0.4	3×10^{-6}	-4.6×10^{-4}	2.9×10^{-2}	-0.96	1.8×10^1	-1.7×10^2	6.7×10^2
F110W	log SNR-J	0.42						-0.25	6.63
F140W	log SNR-J	0.46						-0.27	7.1
F160W	log SNR-J	0.45						-0.25	6.69

Table 4. Galaxy Model Parameters

Parameter	Description	Value	Reference
ρ_0	local UCD population	0.0055 pc^{-3}	Reid et al. (1999)
R_\odot	radial coordinate of the sun	8000 pc	Jurić et al. (2008)
Z_\odot	z coordinate of the sun	25 pc	Jurić et al. (2008)
H_{thick}	thick disk scale height	900 pc	Jurić et al. (2008)
H_{thin}	thin disk scale height	300 pc	Jurić et al. (2008)
L_{thick}	thick disk scale length	3600 pc	Jurić et al. (2008)
L_{thin}	thin disk scale length	2600 pc	Jurić et al. (2008)
p	halo power law index	2.77	Jurić et al. (2008)
q	halo sphere flattening parameter	0.64	Jurić et al. (2008)
f_{thick}	relative number of thick disk stars	0.12	Jurić et al. (2008)
f_{halo}	relative number of halo stars	0.0051	Jurić et al. (2008)

Bardalez Gagliuffi, D. C., Burgasser, A. J.,
Schmidt, S. J., et al. 2019, arXiv e-prints,
arXiv:1906.04166

Basri, G. 1998, in Astronomical Society of the
Pacific Conference Series, Vol. 134, Brown
Dwarfs and Extrasolar Planets, ed. R. Rebolo,
E. Martin, & M. Zapatero Osorio, 394–+

Bastian, N., Covey, K., & Meyer, M. 2010, \araa,
48, 339

Bochanski, J., Hawley, S., Covey, K., et al. 2010,
\aj, 139, 2679

Brammer, G., van Dokkum, P., Franx, M., et al.
2012, \apjs, 200, 13

Table 5. Number Densities. Nex1 is the expected number with a uniform age distribution without selection effects, Nex2 is the expected number with a uniform age distribution taking selection effects into account and Nobs is the number in UCDs with that spectral type in the sample

SpT	Volume (pc^3)	Nex1	Nex2	Nobs
L0	13399.0	22.1	4.1	8
L1	10935.0	17.0	8.9	1
L2	8859.0	11.6	6.4	0
L3	7177.0	9.4	4.6	4
L4	5840.0	7.3	4.3	0
L5	4753.0	5.4	3.4	0
L6	3828.0	4.3	2.0	0
L7	3025.0	3.3	1.0	1
L8	2346.0	2.5	0.8	0
L9	1806.0	1.6	0.7	1
T0	1411.0	1.0	0.6	0
T1	1142.0	0.8	0.5	0
T2	969.0	0.9	0.5	0
T3	854.0	1.1	0.5	1
T4	753.0	1.5	0.7	0
T5	611.0	1.9	1.0	1
T6	400.0	2.0	1.1	1

Burgasser, A. 2001, PhD thesis, AA(Department of Physics, California Institute of Technology)
— . 2004, *\apjs*, 155, 191
— . 2007, *\apj*, 659, 655
— . 2014a, ArXiv e-prints, arXiv:1406.4887

Burgasser, A., Geballe, T., Leggett, S., Kirkpatrick, J., & Golimowski, D. 2006, *\apj*, 637, 1067
Burgasser, A., Looper, D., Kirkpatrick, J., & Liu, M. 2007, *\apj*, 658, 557

- Burgasser, A., Witte, S., Helling, C., et al. 2009, *\apj*, 697, 148
- Burgasser, A. J. 2014b, arXiv:1406.4887
- Burningham, B., Cardoso, C., Smith, L., et al. 2013, *\mnras*, 433, 457
- Burrows, A., Hubbard, W., Lunine, J., & Liebert, J. 2001, *Reviews of Modern Physics*, 73, 719
- Carnero Rosell, A., Santiago, B., dal Ponte, M., et al. 2019, arXiv e-prints, arXiv:1903.10806
- Chabrier, G. 2001, *\apj*, 554, 1274
- Chabrier, G., & Baraffe, I. 2000, *\araa*, 38, 337
- Chabrier, G., & Mera, D. 1997, *A&A*, 328, 83
- Collaboration, T. A., Robitaille, T. P., Tollerud, E. J., et al. 2013, arXiv:1307.6212
- Cruz, K., Reid, I., Kirkpatrick, J., et al. 2007, *\aj*, 133, 439
- Cushing, M., Tokunaga, A., & Kobayashi, N. 2000, *\aj*, 119, 3019
- Cushing, M., Kirkpatrick, J., Gelino, C., et al. 2011, *\apj*, 743, 50
- Davis, M., Guhathakurta, P., Konidaris, N. P., et al. 2007, *The Astrophysical Journal Letters*, 660, L1
- Day-Jones, A., Marocco, F., Pinfield, D., et al. 2013, *\mnras*, 430, 1171
- Delfosse, X., Tinney, C. G., Forveille, T., et al. 1999, *Astron. Astrophys. Suppl. Ser.*, 135, 41
- Dupuy, T., & Liu, M. 2012, *\apjs*, 201, 19
- Faherty, J. K., Bochanski, J. J., Gagne, J., et al. 2018, *The Astrophysical Journal*, 863, 91
- Filippazzo, J. C., Rice, E. L., Faherty, J., et al. 2015, *Astrophysical Journal*, 810, 158
- Gagné, J., Faherty, J. K., Cruz, K. L., et al. 2015, arXiv:1506.07712
- Giavalisco, M., Ferguson, H. C., Koekemoer, A. M., et al. 2004, *The Astrophysical Journal*, 600, L93
- Gould, A., Bahcall, J., & Flynn, C. 1997, *\apj*, 482, 913
- Hardegree-Ullman, K. K., Cushing, M. C., Muirhead, P. S., & Christiansen, J. L. 2019, arXiv e-prints, arXiv:1905.05900
- Holwerda, B. W., Trenti, M., Clarkson, W., et al. 2014, *The Astrophysical Journal*, 788, 77
- Jones, E., Oliphant, T., Peterson, P., et al. 2001–, *SciPy: Open source scientific tools for Python*, , [Online; accessed ;today;]
- Jurić, M., Ivezić, Ž., Brooks, A., et al. 2008, *\apj*, 673, 864
- Kerins, E. J. 1997, *A&A*, 328, 5
- Kimble, R. A., MacKenty, J. W., O’Connell, R. W., & Townsend, J. A. 2008, *Wide Field Camera 3: a powerful new imager for the Hubble Space Telescope*, , doi:10.1117/12.789581
- Kirkpatrick, J. 2005, *\araa*, 43, 195
- Kirkpatrick, J., Looper, D., Burgasser, A., et al. 2010, *\apjs*, 190, 100
- Kirkpatrick, J., Cushing, M., Gelino, C., et al. 2011, *\apjs*, 197, 19
- Kirkpatrick, J. D., Reid, I. N., Liebert, J., et al. 2000, *The Astronomical Journal*, 120, 447
- Kirkpatrick, J. D., Martin, E. C., Smart, R. L., et al. 2019, *ApJS*, 240, 19

- Kümmel, M., Walsh, J. R., Pirzkal, N., Kuntschner, H., & Pasquali, A. 2009, Publications of the Astronomical Society of the Pacific, 121, 59
- Kuntschner, H., Kümmel, M., & Walsh, J. R. 2013
- Lawrence, A., & Others. 2007, *\mnras*, 379, 1599
- Lodieu, N., Espinoza Contreras, M., Zapatero Osorio, M. R., et al. 2017, *Astronomy & Astrophysics*, 598, A92
- Lopez-Santiago, J., Montes, D., Crespo-Chacon, I., & Fernandez-Figueroa, M. J. 2006, *The Astrophysical Journal*, 643, 1160
- LSST Science Collaboration, L. S., Abell, P. A., Allison, J., et al. 2009, arXiv:0912.0201
- Luhman, K. L., & Mamajek, E. E. 2012, *The Astrophysical Journal*, 758, 31
- Mamajek, E. E. 2015, *Proceedings of the International Astronomical Union*, 10, 21
- Manjavacas, E., Apai, D., Zhou, Y., et al. 2018, arXiv:1812.03963
- Marocco, F., Jones, H. R. A., Day-Jones, A. C., et al. 2015, *Monthly Notices of the Royal Astronomical Society*, 449, 3651
- Martin, E. C., Mace, G. N., McLean, I. S., et al. 2017, *The Astrophysical Journal*, 838, 73
- Masters, D., McCarthy, P., Burgasser, A., et al. 2012, *\apjl*, 752, L14
- Metchev, S., Kirkpatrick, J., Berriman, G., &Looper, D. 2008, *\apj*, 676, 1281
- Miller, A. A., Kulkarni, M. K., Cao, Y., et al. 2017, *The Astronomical Journal*, 153, 73
- Momcheva, I. G., Brammer, G. B., van Dokkum, P. G., et al. 2016, *The Astrophysical Journal Supplement Series*, 225, 27
- Pedregosa, F., Varoquaux, G., Gramfort, A., et al. 2012, arXiv e-prints, arXiv:1201.0490
- Pirzkal, N., Sahu, K., Burgasser, A., et al. 2005, *\apj*, 622, 319
- Pirzkal, N., Burgasser, A., Malhotra, S., et al. 2009, *\apj*, 695, 1591
- Reid, I., Kirkpatrick, J., Liebert, J., et al. 1999, *\apj*, 521, 613
- Reylé, C. 2018, *Astronomy & Astrophysics*, 619, L8
- Reylé, C., & Robin, A. C. 2001, *A&A*, 373, 886
- Reyle, C., Delorme, P., Willott, C. J., et al. 2010, *Astronomy and Astrophysics*, Volume 522, id.A112, 15 pp., 522, arXiv:1008.2301
- Rujopakarn, W., Eisenstein, D. J., Rieke, G. H., et al. 2010, *ApJ*, 718, 1171
- Ryan, R. E., Thorman, P. A., Yan, H., et al. 2011, *The Astrophysical Journal*, 739, 83
- Ryan, R. E., Thorman, P. A., Schmidt, S. J., et al. 2017, *The Astrophysical Journal*, 847, 53
- Ryan Jr., R., Hathi, N., Cohen, S., & Windhorst, R. 2005, *\apjl*, 631, L159
- Ryan Jr., R. E., & Reid, I. N. 2016, *The Astronomical Journal*, 151, 92
- Schneider, A. C., Cushing, M. C., Kirkpatrick, J. D., et al. 2015, *The Astrophysical Journal*, 804, 92
- Scoville, N., Aussel, H., Brusa, M., et al. 2007, *The Astrophysical Journal Supplement Series*, 172, 1

- Skelton, R. E., Whitaker, K. E., Momcheva, I. G., et al. 2014, *The Astrophysical Journal Supplement Series*, 214, 24
- Sorahana, S., Nakajima, T., & Matsuoka, Y. 2018, arXiv:1811.07496
- Spergel, D., Gehrels, N., Baltay, C., et al. 2015, arXiv:1503.03757
- Tokunaga, A., & Kobayashi, N. 1999, *AJ*, 117, 1010
- Van Vledder, I., Van Der Vlugt, D., Holwerda, B. W., et al. 2016, *Monthly Notices of the Royal Astronomical Society*, 458, 425
- Zhang, Z. H., Burgasser, A. J., Gálvez-Ortiz, M. C., et al. 2019, *MNRAS*, 486, 1260